Assessment of body force effects in flow condensation, part II: Criteria for negating influence of gravity

Lucas E. O'Neill, Ilchung Park, Chirag R. Kharangate, V.S. Devahdhanush, V. Ganesan, Issam Mudawar *

Boiling and Two-Phase Flow Laboratory (BTPFL), School of Mechanical Engineering, Purdue University, 585 Purdue Mall, West Lafayette, IN 47907, USA

ABSTRACT

This study concerns the development of a set of mechanistic criteria capable of predicting the flow conditions for which gravity independent flow condensation heat transfer can be achieved. Using FC-72 as working fluid, a control-volume based annular flow model is solved numerically to provide information regarding the magnitude of different forces acting on the liquid film and identify which forces are dominant for different flow conditions. Separating the influence of body force into two components, one parallel to flow direction and one perpendicular, conclusions drawn from the force term comparison are used to model limiting cases, which are interpreted as transition points for gravity independence. Experimental results for vertical upflow, vertical downflow, and horizontal flow condensation heat transfer coefficients are presented, and show that, for the given test section, mass velocities above 425 kg/m^2 s ensure gravity independent heat transfer. Parametric evaluation of the criteria using different assumed values of mass velocity, orientation, local acceleration, and exit quality show that the criteria obey physically verifiable trends in line with those exhibited by the experimental results. As an extension, the separated flow model is utilized to provide a more sophisticated approach to determining whether a given configuration will perform independent of gravity. Results from the model show good qualitative agreement with experimental results. Additionally, analysis of trends indicate use of the separated flow model captures physics missed by simpler approaches, demonstrating that use of the separated flow model with the gravity independence criteria constitute a powerful predictive tool for engineers concerned with ensuring gravity independent flow condensation heat transfer performance.

© 2016 Elsevier Ltd. All rights reserved.

1. Introduction

1.1. Transitioning from single-phase to two-phase thermal management systems

In recent years, increased heat dissipation from electronic and power devices, coupled with their shrinking size has motivated engineers to develop compact thermal management systems capable of handling the acquisition and rejection of high heat fluxes. These systems are critical to such applications as high performance computers, hybrid vehicle power electronics, directed energy laser and microwave weapons, and avionics for next generation aircraft and spacecraft [1]. Because to their ability to capitalize on a coolant's latent as well as sensible heat, two-phase thermal management systems can yield orders of magnitude enhancement in

heat transfer performance over their single phase counterparts, making them ideally suited for thermal management of high heat flux devices and systems.

Many previous studies have been focused on proposed configurations for heat acquisition by boiling, including pool boiling [2], channel flow boiling [3–5], jet [6,7] and spray [8–10], some have investigated mechanisms for heat rejection by condensation, including flow condensation in circular channels [11–13] and rectangular channels [14], but only a select few have focused on ensuring two-phase thermal management systems perform independent of body force effects caused by system orientation and local gravitational acceleration.

The magnitude of body force is an important factor when considering two-phase thermal management, as the orders of magnitude difference between liquid and vapor densities creates significant buoyancy effects relative to those encountered in traditional single-phase thermal management systems. If unmitigated, body force effects can lead to widely varying heat transfer performance with respect to system orientation.

* Corresponding author. Fax: +1 (765) 494 0539.
  E-mail address: mudawar@ecn.purdue.edu (I. Mudawar).
  URL: https://engineering.purdue.edu/BTPFL (I. Mudawar).

Nomenclature

a	local acceleration (body force per unit mass); empirical constant
A^+	parameter in eddy diffusivity relation
$A_{f,*}$	flow area of liquid control volume
Bo	Bond number
c	wave speed
c_i	imaginary component of wave speed
c_p	specific heat at constant pressure
c_r	real component of wave speed
D	diameter
D_F	characteristic length scale
D_H	hydraulic diameter
f_i	interfacial friction factor
Fr	Froude number
G	mass velocity
g	gravity
h	heat transfer coefficient
H_f	thickness of liquid layer
H_g	thickness of vapor layer
K	Von-Karman constant
k	wave number
k_c	critical wave number
L_{char}	characteristic length
$\dot{m}$	mass flow rate
n	empirical exponent
P	pressure; perimeter
P_f	friction perimeter
Pr	Prandtl number
Pr_T	turbulent Prandtl number
q''	heat flux
q_w''	wall heat flux
Re_c	vapor core Reynolds number
T	temperature
t	time
T^+	dimensionless temperature
u	velocity
u^*	friction velocity
U_{char}	characteristic velocity

We	Weber number
x_e	thermodynamic equilibrium quality
y	coordinate perpendicular to wall
y^+	dimensionless coordinate perpendicular to wall
z	axial coordinate

Greek symbols

α	void fraction
Γ_{fg}	rate of condensation mass transfer per unit length
δ	mean thickness of liquid film
δ^+	dimensionless mean thickness of liquid film
ε	eddy momentum diffusivity
η	interfacial perturbation
η_0	amplitude of interfacial perturbation
λ	wavelength
λ_c	critical wavelength
μ	dynamic viscosity
v	kinematic viscosity
ρ	density
ρ''	modified density
σ	surface tension
τ	shear stress
θ	channel orientation angle

Subscripts

c	critical
$char$	characteristic
f	liquid
FC	FC-72
g	vapor
i	interfacial
in	inlet to heat transfer measurement length
out	outlet of heat transfer measurement length
sat	saturation
tp	two phase
w	wall; water

1.2. Mitigating body force effects

For flow boiling, a study by Zhang et al. [15] established a set of dimensionless groups capable of predicting at what inlet mass velocities the value of critical heat flux (CHF) would be independent of gravity. His work was later expanded by Konishi et al. [16] to determine gravity independence in cases with finite inlet quality.

Several flow condensation studies have addressed the effects of orientation on condensation heat transfer coefficient [17,18], with a small number focusing on flow condensation in microgravity [19,20], but a systematic approach to mitigating the influence of gravity on flow condensation heat transfer utilizing criteria composed of dimensionless groups is a current deficiency in available literature.

Were such a predictive tool available, it would be highly instrumental in the design of thermal management systems for such important applications as aircraft avionics, spacecraft avionics and power systems, and other applications where a wide range of local accelerations and system orientations are expected. Currently, thermal design engineers are limited in their ability to predict the threshold mass velocity of working fluid required for gravity independent flow condensation heat transfer, leading them to either confirm gravity independence through expensive experiments or utilize unnecessarily high mass velocities and oversized pumps.

1.3. Objectives of study

For the reasons discussed above, it is the primary goal of this second part of a two-part study to develop a set of mechanistic criteria comprised of relevant dimensionless groups that are capable of predicting the onset of gravity independent flow condensation heat transfer. In the first part [21], the influence of gravity on flow condensation was isolated by conducting identical experiments in horizontal flow, vertical downflow, and vertical upflow orientations using FC-72 as working fluid. In this second part, the experimental findings from the first part are used to develop the mechanistic criteria for negating the influence of gravity in condensing flows.

The present study is part of a joint project between the Purdue University Boiling and Two-Phase Flow Laboratory (PU-BTPFL) and NASA Glenn Research Center whose ultimate goal is to develop the Flow Boiling and Condensation Experiment (FBCE) for the International Space Station (ISS). Key goals for the ISS project are to amass flow boiling and condensation databases in microgravity, and to develop mechanistic criteria for negating the influence of gravity

on flow boiling critical heat flux (CHF) and flow condensation in microgravity.

2. Experimental methods

Fig. 1(a) shows a schematic diagram of the condensation facility utilized for this study. The facility consists of three flow loops: a primary loop for the working fluid, FC-72, and two separate water cooling loops. A 14.2 kW Watlow pre-heater in the primary loop is used to convert liquid FC-72 to a slightly superheated state before entering the condensation module, which is the main component of the facility. Within the condensation module, FC-72 vapor passing through a central stainless steel tube is condensed by rejecting

heat to a counter flow of cooling water through an annulus surrounding the central tube. The cooling water is circulated by the first water cooling loop, consisting of a 14-kW modular Lytron LCS cooling system which absorbs heat from the FC-72 and rejects it to tap water using a liquid-to-liquid heat exchanger. The second water cooling loop consists of a 1.46-kW modular Lytron system which fully condenses any residual FC-72 exiting the condensation module and rejects the heat to ambient air a water-to-air heat exchanger.

Fig. 1(b) illustrates the construction of the condensation test module, which features two concentric tubes made of 304 stainless steel and a total condensation length of 1259.8 mm. The inner FC-72 tube has an inner diameter of 11.89 mm and 0.41-mm wall thickness, and the outer water tube has an inner diameter of
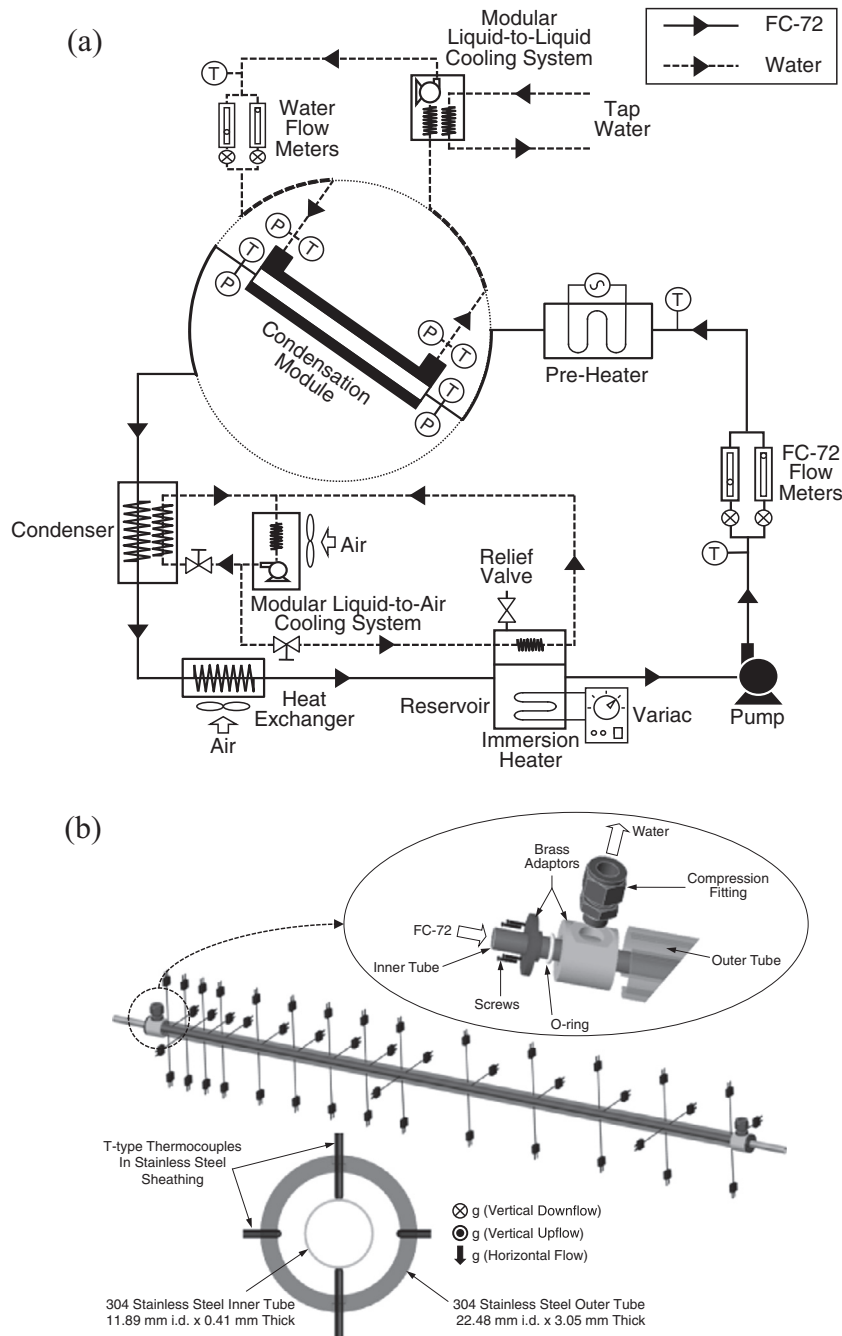

Fig. 1. (a) Schematic diagram of condensation facility. (b) Construction of condensation heat transfer test module.

22.48 mm and 3.05-mm wall thickness. A thick layer of fiberglass insulation is applied over the entire condensation module to minimize heat loss to the ambient.

In addition to the temperature and pressure measurements made at the FC-72 and water inlets and outlets of the condensation module, 45 type-T thermocouples are used to measure the inner tube's outer wall temperature and the water temperature. 28 thermocouples are installed in 14 diametrically opposite pairs on the outer wall of the inner tube. 14 Additional thermocouples are inserted into the annulus at the same axial locations as the wall thermocouples to measure the water temperatures. Finally, three of the 14 water axial measurement locations contain an additional thermocouple mounted diametrically opposite to the main thermocouple to capture any circumferential nonuniformities in the water temperature. The spacing between axial thermocouple measurement locations ranges from a minimum 38.1 mm near the inlet, to 76.2 mm in the middle, and 139.7 mm near the outlet.

The test matrix consists of 39 sets of operating conditions including three orientations: horizontal flow, vertical downflow and vertical upflow. The operating conditions consist of thirteen FC-72 mass velocities in the range of G_{FC} = 116.80–576.83 kg/m^2 s, and three water mass velocities of G_w = 246.66, 277.48, and 308.32 kg/m^2 s for each FC-72 mass velocity. To avoid any potential uncertainties due to cooling water entrance effects, heat transfer data are only collected within the upstream condensation length of z = 0–807.7 mm. The inlet quality of FC-72 is slightly superheated for all test cases. Inlet temperatures and pressures fall within the range of $T_{FC,in}$ = 63.06–84.46 °C and $P_{FC,\ in}$ = 99.73–205.00 kPa for all three orientations.

Additional details on the experimental methods used, including uncertainty analysis, are provided in the first part of the study [21].

3. Analysis of forces on liquid film

3.1. Impact of liquid film development on condensation heat transfer

In annular flow condensation, a liquid film blankets the cooling surface, surrounding a saturated vapor core that condenses gradually along the liquid film's interface. The condensation heat transfer coefficient is dependent on local thickness of the liquid film as well as turbulence intensity within the film; the latter is reflected in the film's velocity profile. The rate of condensation is driven by the temperature gradient across the interface and the cooling wall.

Large heat transfer coefficients are realized in the upstream region of a condensing tube, where the liquid film is thinnest and vapor core velocity highest, and can also be enhanced by increased turbulence intensity as the film thickens along the flow direction. Therefore, any criteria aiming to establish gravity independent condensation heat transfer must address the hydrodynamic development of the liquid film. In order for the flow to be gravity independent, the film must exhibit both circumferential symmetry and identical axial development for all orientations. As gravity is the only force that varies with orientation of the test section, a condition for establishing circumferential symmetry and identical axial development of the liquid film must be that the influence of body force is negligible compared to that of the other forces acting on the film.

3.2. Use of separated flow model to analyze forces acting on liquid film

Relative magnitude of gravitational force to that of the other forces acting on the liquid film is key to determining when the liquid film is no longer influenced by gravity. Although many prior studies have culminated in correlations capable of accurately predicting condensation heat transfer performance [22,23], these correlations do not provide the means to determine the different forces acting on the liquid film. A more effective method to determining these forces for different flow conditions is to construct a separated flow, control-volume-based model for annular flow. This type of model was recently developed for vertical downflow condensation [24], and later modified for horizontal flow condensation [25], and vertical upflow condensation [26]. A summary of the model's key equations is provided in Table 1, with full details of the model's construction provided by Park et al. [24].

Fig. 2(a)–(c) shows control volumes encompassing a portion of the liquid film and the forces acting on the control volume for horizontal flow, vertical downflow, and vertical upflow, respectively. The flow parameters governing the magnitude of the forces are the rate of interfacial mass transfer due to condensation per unit distance, Γ_{fg}, interfacial velocity, u_i, axial pressure gradient, $-dP/dz$, interfacial shear stress, τ_i, wall shear stress, τ_w, and gravity, g. Utilizing the separated flow, control-volume-based model, the magnitudes of forces per unit length acting on the liquid film are computed. It is important to note that gravity is neglected for horizontal flow based on the assumption of circumferentially symmetric liquid film. Symmetry is intended here only for comparative purposes, and stratification effects specific to horizontal flow will be discussed detail later. As discussed in [24], axial momentum changes of the liquid film are negligible, and therefore ignored in the model development.

Fig. 3(a)–(e) shows axial variations of the magnitude of forces per unit length for a control volume encompassing the entire liquid film ($y = \delta$ in Fig. 2(a)–(c)) corresponding to five sets of operating conditions and three flow orientations. They include:

1. Momentum transfer per unit length from the vapor core to the liquid film, $\Gamma_{fg} u_i$.
2. Force per unit length due to the pressure gradient, $(dP/dz)A_{f,*}|_{y=0}$, where $A_{f,*}|_{y=0} = (\pi/4)[D^2 - (D - 2\delta)^2]$ is the cross-sectional area of liquid film.
3. Interfacial shear force per unit length, $\tau_i P_{f,\delta}$, where $P_{f,\delta} = \pi(D - 2\delta)$ is the interfacial perimeter.
4. Wall shear force per unit length, $\tau_w P_{f,y}|_{y=0}$, where $P_{f,y}|_{y=0} = \pi D$ is the film's outer perimeter.
5. Body force per unit length, $\rho_f A_{f,*}|_{y=0}|g \sin \theta|$, where $A_{f,*}|_{y=0} = (\pi/4)[D^2 - (D - 2\delta)^2]$ is the cross sectional area of the liquid film, and $|g \sin \theta| = 0$ for horizontal flow, $|g \sin \theta| = g$ for vertical downflow and vertical upflow.

It should be noted that the vertical upflow cases are provided only for the two highest mass velocities tested due to the model's inability to converge for vertical upflow with low mass velocities [26]. Fig. 3(a)–(e) shows the magnitude of force per unit length due to the axial pressure gradient is comparatively quite small for all FC-72 mass velocities and flow orientations. The interfacial momentum transfer is also comparatively small for all flow orientations, but increases with increasing FC-72 mass velocity due to the increase in u_i, and exhibits a peak a short distance downstream from the inlet where the rate of condensation is highest. In the upstream region, wall shear force is the most dominant for all orientations and mass velocities due to the sharp velocity gradient near the wall, but decreases gradually in the flow direction. The rate at which wall shear force decreases axially is highest for vertical upflow, where gravity is acting to retard fluid motion, and lowest for vertical downflow, where gravity is assisting fluid motion. The magnitude of interfacial shear force follows a trend similar to that of wall shear force, with maximum value in the upstream region and a continuous decrease along the channel length. It is important to note that while wall shear force maintains a slightly larger magnitude than interfacial shear force for

Table 1
Annular flow model relations [24].

Mass conservation

$$\frac{d\dot{m}_f}{dz} - \Gamma_{fg} = 0; \; \frac{d\dot{m}_g}{dz} + \Gamma_{fg} = 0; \; \dot{m}_f = \rho_f \int_0^\delta u_f \pi(D-2y)dy; \; \dot{m}_g = \rho_g \bar{u}_g \pi(D-2\delta)^2/4; \; \Gamma_{fg} = q_w'' \pi D/h_{fg}$$

Momentum conservation for liquid film

$$\tau = \mu_f\left(1 + \frac{\varepsilon_m}{\nu_f}\right)\frac{du_f}{dy} = \left(-\frac{dp}{dz}\right)\frac{A_{f,*}}{P_{f,y}} + \frac{\tau_i P_{f,\delta} + \Gamma_{fg} u_i}{P_{f,y}} \quad (Horizontal\; Flow)$$

$$= \left(-\frac{dp}{dz} + \rho_f g\right)\frac{A_{f,*}}{P_{f,y}} + \frac{\tau_i P_{f,\delta} + \Gamma_{fg} u_i}{P_{f,y}} \quad (Vertical\; Downflow)$$

$$= \left(-\frac{dp}{dz} - \rho_f g\right)\frac{A_{f,*}}{P_{f,y}} + \frac{\tau_i P_{f,\delta} + \Gamma_{fg} u_i}{P_{f,y}} \quad (Vertical\; Upflow)$$

$$A_{f,*} = \frac{\pi}{4}(D-2y)^2 - \frac{\pi}{4}(D-2\delta)^2, \; P_{f,y} = \pi(D-2y), \; P_{f,\delta} = \pi(D-2\delta)$$

Velocity profile across film

$$u_f(y) = \frac{\delta}{\mu_f}\left(-\frac{dP}{dz}\right)\int_0^{y/\delta}\frac{A_{f,*}}{P_{f,y}}\left(1+\frac{\varepsilon_m}{\nu_f}\right)^{-1}d\left(\frac{y}{\delta}\right) + \frac{\delta}{\mu_f}(\tau_i P_{f,\delta} + \Gamma_{fg} u_i)\int_0^{y/\delta}\frac{1}{P_{f,y}}\left(1+\frac{\varepsilon_m}{\nu_f}\right)^{-1}d\left(\frac{y}{\delta}\right) \quad (Horizontal\; Flow)$$

$$= \frac{\delta}{\mu_f}\left(-\frac{dP}{dz}+\rho_f g\right)\int_0^{y/\delta}\frac{A_{f,*}}{P_{f,y}}\left(1+\frac{\varepsilon_m}{\nu_f}\right)^{-1}d\left(\frac{y}{\delta}\right) + \frac{\delta}{\mu_f}(\tau_i P_{f,\delta} + \Gamma_{fg} u_i)\int_0^{y/\delta}\frac{1}{P_{f,y}}\left(1+\frac{\varepsilon_m}{\nu_f}\right)^{-1}d\left(\frac{y}{\delta}\right) \quad (Vertical\; Downflow)$$

$$= \frac{\delta}{\mu_f}\left(-\frac{dP}{dz}-rho_f g\right)\int_0^{y/\delta}\frac{A_{f,*}}{P_{f,y}}\left(1+\frac{\varepsilon_m}{\nu_f}\right)^{-1}d\left(\frac{y}{\delta}\right) + \frac{\delta}{\mu_f}(\tau_i P_{f,\delta} + \Gamma_{fg} u_i)\int_0^{y/\delta}\frac{1}{P_{f,y}}\left(1+\frac{\varepsilon_m}{\nu_f}\right)^{-1}d\left(\frac{y}{\delta}\right) \quad (Vertical\; Upflow)$$

$$u_i = u_f(\delta)$$

Pressure gradient

$$-\frac{dP}{dz} = \frac{\frac{\mu_f \dot{m}_f}{\rho_f \delta^2} - (\tau_i P_{f,\delta} + \Gamma_{fg} u_i)\int_0^1\left[P_{f,y}\int_0^{y/\delta}\frac{1}{P_{f,y}}\left(1+\frac{\varepsilon_m}{\nu_f}\right)^{-1}d\left(\frac{y}{\delta}\right)\right]d\left(\frac{y}{\delta}\right)}{\int_0^1\left[P_{f,y}\int_0^{y/\delta}\frac{A_{f,*}}{P_{f,y}}\left(1+\frac{\varepsilon_m}{\nu_f}\right)^{-1}d\left(\frac{y}{\delta}\right)\right]d\left(\frac{y}{\delta}\right)} \quad (Horizontal\; Flow)$$

$$= -\rho_f g + \frac{\frac{\mu_f \dot{m}_f}{\rho_f \delta^2} - (\tau_i P_{f,\delta} + \Gamma_{fg} u_i)\int_0^1\left[P_{f,y}\int_0^{y/\delta}\frac{1}{P_{f,y}}\left(1+\frac{\varepsilon_m}{\nu_f}\right)^{-1}d\left(\frac{y}{\delta}\right)\right]d\left(\frac{y}{\delta}\right)}{\int_0^1\left[P_{f,y}\int_0^{y/\delta}\frac{A_{f,*}}{P_{f,y}}\left(1+\frac{\varepsilon_m}{\nu_f}\right)^{-1}d\left(\frac{y}{\delta}\right)\right]d\left(\frac{y}{\delta}\right)} \quad (Vertical\; Downflow)$$

$$= \rho_f g + \frac{\frac{\mu_f \dot{m}_f}{\rho_f \delta^2} - (\tau_i P_{f,\delta} + \Gamma_{fg} u_i)\int_0^1\left[P_{f,y}\int_0^{y/\delta}\frac{1}{P_{f,y}}\left(1+\frac{\varepsilon_m}{\nu_f}\right)^{-1}d\left(\frac{y}{\delta}\right)\right]d\left(\frac{y}{\delta}\right)}{\int_0^1\left[P_{f,y}\int_0^{y/\delta}\frac{A_{f,*}}{P_{f,y}}\left(1+\frac{\varepsilon_m}{\nu_f}\right)^{-1}d\left(\frac{y}{\delta}\right)\right]d\left(\frac{y}{\delta}\right)} \quad (Vertical\; Upflow)$$

Momentum conservation for vapor core

$$\tau_i = \frac{1}{P_{f,\delta}}\left[A_g\left(-\frac{dP}{dz}\right) - \frac{d(\rho_g \bar{u}_g^2 A_g)}{dz} - \Gamma_{fg} u_i\right] \quad (Horizontal\; Flow)$$

$$= \frac{1}{P_{f,\delta}}\left[A_g\left(-\frac{dP}{dz}+\rho_f g\right) - \frac{d(\rho_g \bar{u}_g^2 A_g)}{dz} - \Gamma_{fg} u_i\right] \quad (Vertical\; Downflow)$$

$$= \frac{1}{P_{f,\delta}}\left[A_g\left(-\frac{dP}{dz}-\rho_f g\right) - \frac{d(\rho_g \bar{u}_g^2 A_g)}{dz} - \Gamma_{fg} u_i\right] \quad (Vertical\; Upflow)$$

$$A_g = \pi(D-2\delta)^2/4$$

Interfacial shear stress relation [27,28]

$$\tau_i = \frac{1}{2}f_i \rho_g (\bar{u}_g - u_i)^2 + \frac{(\bar{u}_g - u_i)\Gamma_{fg}}{2P_{f,\delta}}$$

$$f_i = 16/Re_c \; for \; Re_c < 2000; \quad f_i = 0.079 Re_c^{-0.25} \; for \; 2000 \leqslant Re_c < 20,000,$$

$$f_i = 0.046 Re_c^{-0.2} \; for \; Re_c \geqslant 20,000; \quad Re_c = \rho_g(\bar{u}_g - u_i)(D-2\delta)/\mu_g$$

Eddy momentum diffusivity [29]

$$\frac{\varepsilon_m}{\nu_f} = -\frac{1}{2} + \frac{1}{2}\sqrt{1 + 4K^2 y^{+2}\left[1 - \exp\left(-\sqrt{1-\frac{y^+}{\delta^+}}\frac{y^+}{A^+}\right)\right]^2\left(1-\frac{y^+}{\delta^+}\right)\frac{\tau}{\tau_w}}; \quad K = 0.4; \; A^+ = 26\left(1 + 30.18\mu_f \rho_f^{-0.5}\tau_w^{-1.5}\frac{dP}{dz}\right)^{-1}$$

Turbulent Prandtl number [30]

$$Pr_T = 1.4 \exp\left(-15\frac{y^+}{\delta^+}\right) + 0.66; \quad \delta^+ = \delta u^*/\nu_f$$

Heat transfer coefficient

$$h = \frac{q_w''}{T_{sat}-T_w} = \frac{\rho_f c_{pf} u^*}{T_\delta^+} = \frac{\rho_f c_{pf} u^*}{\int_0^{\delta^+}\frac{q''}{q_w''}\left(\frac{1}{Pr_f}+\frac{1}{Pr_T}\frac{\varepsilon_m}{\nu_f}\right)^{-1}dy^+} = \frac{\rho_f c_{pf} u^*}{\int_0^{\delta^+}\left(\frac{D}{D-2\delta}\right)\left(\frac{1}{Pr_f}+\frac{1}{Pr_T}\frac{\varepsilon_m}{\nu_f}\right)^{-1}dy^+}$$

horizontal and vertical downflow orientations, the model predictions show that, for vertical upflow, interfacial shear force surpasses wall shear force at a downstream location between $z = 0.2$ and 0.4 m. This is due to gravity slowing the liquid film more significantly than the vapor core, thereby increasing the velocity gradient at the interface while reducing the velocity gradient at the wall.

Expectedly, body force exhibits the greatest complexity among the different orientations. For vertical downflow and vertical upflow, the magnitude of body force increases along the flow direction as the liquid film thickens. For two lowest FC-72 mass velocities, Fig. 3(a) and (b), the magnitude of body force for vertical downflow is relatively quite significant. For $G_{FC} = 348.70$ kg/m^2 s, Fig. 3(c), and $G_{FC} = 463.11$ kg/m^2 s, Fig. 3(d), the magnitude of body force for vertical downflow becomes smaller than that of both wall and interfacial shear forces. For vertical upflow, however, the

magnitude of body force for $G_{FC} = 463.11$ kg/m^2 s exceeds that of interfacial shear force in the downstream region of the condensation tube. This can be explained by the lower film velocity in vertical upflow increasing film thickness at the exit as compared to vertical downflow, rendering body force a more significant contributor compared to vertical downflow.

For the highest FC-72 mass velocities, Fig. 3(d) and (e), the magnitude of body force for vertical downflow follows a trend similar to that in Fig. 3(c). And even at these highest mass velocities, the magnitude of body force for vertical upflow is greater than that of wall shear force in the downstream region, but remains smaller than interfacial shear force over the entire condensation length. For vertical upflow, the direction of interfacial shear force is opposite that of body force, meaning the influence of gravity on condensation is diminished for flow conditions in which the magnitude of interfacial shear force exceeds that of body force.
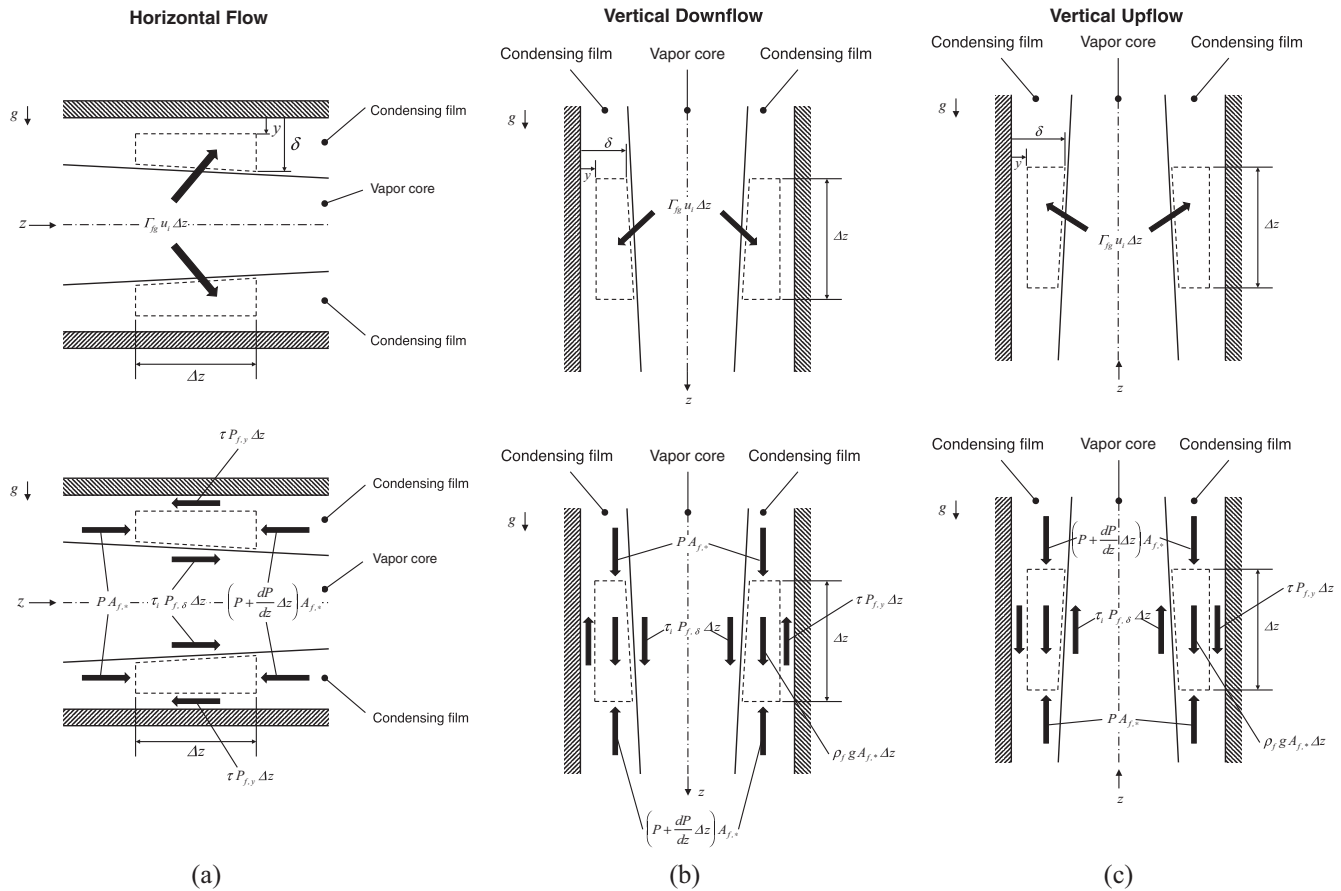
Fig. 2. Momentum and force components of liquid film control volume for (a) horizontal flow, (b) vertical downflow, and (c) vertical upflow.

Overall, Fig. 3(a)–(e) points to the following important trends concerning the magnitude of body force relative to the other forces acting on the control volume:

(i) The film's motion is governed mostly by a balance between wall shear, interfacial shear and body force, with interfacial momentum and axial pressure gradient playing a relatively minor role.

(ii) For both vertical downflow and vertical upflow, the magnitude of body force is highest at the outlet, where the liquid film is thickest. This is also where both wall shear and interfacial shear are lowest along the condensation length.

(iii) Body force is most significant for vertical upflow, where gravity opposes fluid motion and therefore tends to thicken the liquid film. Here, wall shear decreases considerably near the outlet, leaving mostly interfacial shear to balance the body force.

Clearly, these trends are influenced both by the thermophysical properties of FC-72 and operating conditions. The following section will address the influence of body force more thoroughly by taking these trends into account, while aiming to address body force effects in a more universal manner.

4. Methodology for overcoming body force effects on flow condensation heat transfer

As discussed earlier, it is the primary objective of the present study to develop criteria for negating the influence of gravity on flow condensation. Since body force plays drastically different roles depending on flow orientation relative to gravity, the influence of body force is separated into two components: component parallel to or opposite to flow direction, and component perpendicular to flow direction. To mitigate these components two separate criteria are developed, with satisfaction of both criteria indicating flow condensation heat transfer will be independent of gravity. To simplify modeling, all cases are assumed to begin with fully saturated vapor at the channel inlet, $x_{e,in} = 1.0$.

4.1. Component of body force parallel to or opposite flow direction

In vertical and near-vertical orientations, the component of body force parallel to or opposite the flow direction plays a significant role in the development of the liquid film's velocity profile. From previous studies regarding flow regime maps and transition correlations for flow condensation [31–36], it is clear that vertical downflow condensation will remain in the annular flow regime for all inlet velocities until flow quality is reduced to a point where liquid bridging occurs between diametrically opposite locations of the condensation tube and slug flow is established. This behavior is the result of body force aiding film motion for the vertical downflow orientation. For vertical upflow, however, film behavior is dependent on the relative magnitudes of body force and interfacial shear force provided by the vapor core. In situations where body force dominates, falling film behavior is encountered, with the liquid flowing opposite to the vapor flow. In instances where interfacial shear force dominates, co-current annular flow is encountered, where the liquid flows parallel to the vapor flow, similar to that of vertical downflow. For intermediate cases, where
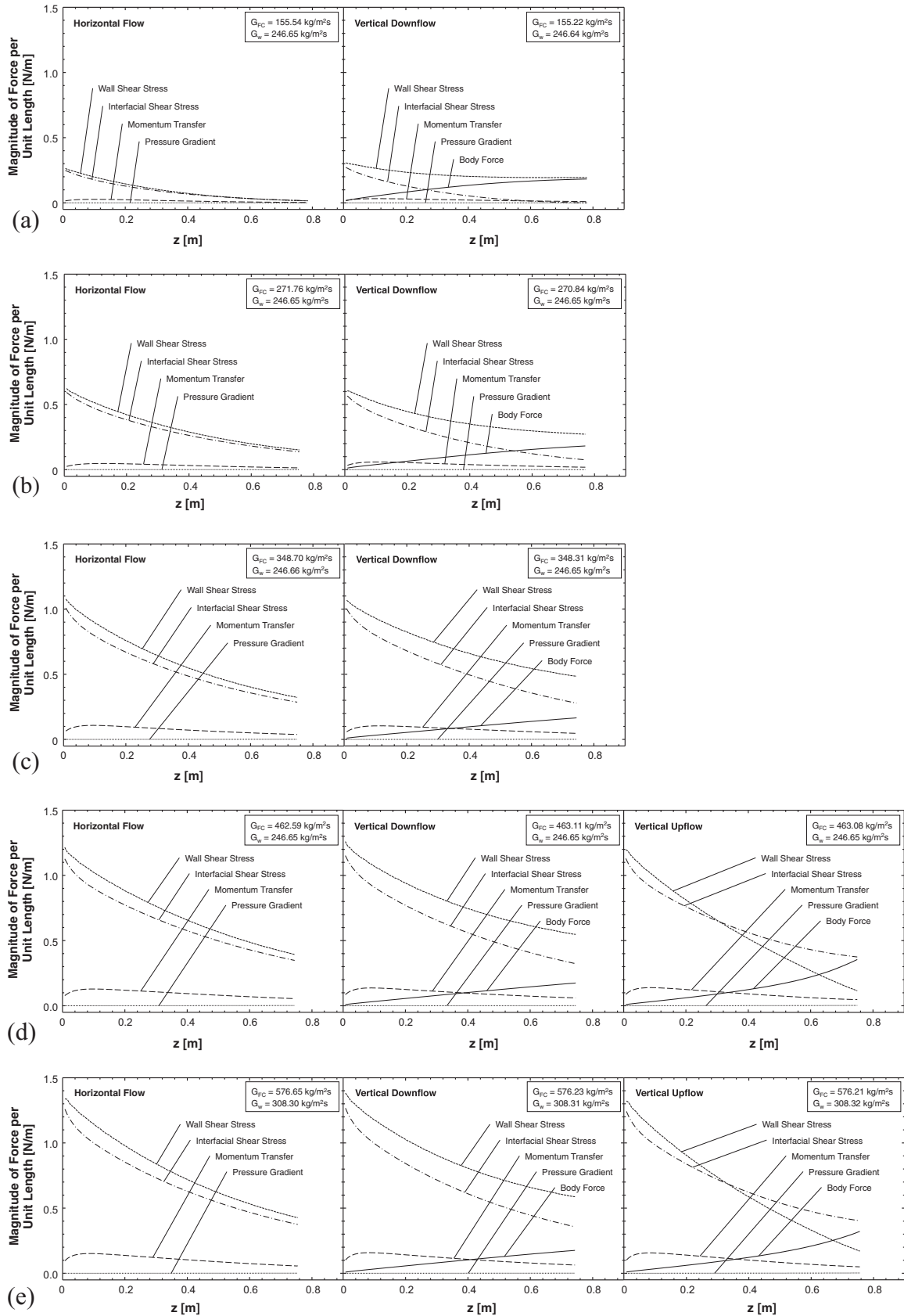
Fig. 3. Axial variations of forces acting on liquid film for (a) G_{FC} = 155.54 kg/m² s, (b) G_{FC} = 271.76 kg/m² s, (c) G_{FC} = 348.70 kg/m² s, (d) G_{FC} = 462.59 kg/m² s, and (e) G_{FC} = 576.65 kg/m² s.

the two forces are comparable, flooding and oscillating film flow regimes are present. In order to achieve condensation heat transfer

independent of the body force component parallel to or opposite to the flow direction, the same co-current annular flow regime must

be present for all orientations. This means that mass velocity must be sufficient to establish co-current annular flow with film and core vapor velocities similar to those seen in vertical downflow for the limiting case of vertical upflow.

To develop a mechanistic criterion capable of predicting the flow conditions required to satisfy this condition, a situation in which the liquid film is beginning to depart from co-current flow and enter the flooding regime is modeled. Fig. 4(a) shows the force balance on the liquid film, comprised of the same force components considered in the previous section, and again making the assumption of a smooth interface. In the case outlined here (onset of flooding), the liquid film is assumed to be nearly stationary, resulting in the relationship for force balance

$$P\pi\frac{D_H^2-(D_H-2\,\delta)^2}{4}+\Gamma_{fg}u_i\Delta z+\tau_i\,\pi\,(D_H-2\,\delta)\,\Delta z$$
$$=\left(P+\frac{dP}{dz}\Delta z\right)\pi\,\frac{D_H^2-(D_H-2\,\delta)^2}{4}$$
$$+\rho_f g\,\pi\frac{D_H^2-(D_H-2\,\delta)^2}{4}\Delta z+\tau_w\,\pi D_H\,\Delta z, \tag{1}$$

where D_H is the hydraulic diameter, which is used to generalize the criterion for body force negation to both circular and non-circular channels. From the analysis of forces included in the separated flow model discussed in the previous section, it is clear that the contribution of pressure gradient and momentum transfer due to phase change across the interface are quite small compared to the other

terms, allowing those terms to be neglected. Also, as discussed in the previous section, the wall shear stress near the outlet corresponding to the onset of flooding decreases considerably, allowing this term to be neglected as well. Fig. 4(b) shows these simplification reduce the force balance to one of interfacial shear supporting the weight of the liquid film, allowing Eq. (1) to simplify to

$$\tau_i(D_H-2\,\delta)=\rho_f g\frac{D_H^2-(D_H-2\,\delta)^2}{4}. \tag{2}$$

The interfacial shear stress can be determined by the Wallis relation [28]

$$\tau_i=\frac{1}{2}f_i\,\rho_g\big(\bar{u}_g-u_i\big)^2+\frac{(\bar{u}_g-u_i)\,\Gamma_{fg}}{2\,\pi(D_H-2\,\delta)}, \tag{3}$$

where f_i and $\bar{u}_g$ are the interfacial friction factor and mean velocity of the vapor core, respectively. Combining Eqs. (2) and (3), and again neglecting the momentum transfer due to phase change across the interface yields

$$\frac{1}{2}f_i\rho_g\big(\bar{u}_g-u_i\big)^2(D_H-2\,\delta)=\rho_f g\frac{D_H^2-(D_H-2\,\delta)^2}{4}. \tag{4}$$

The interfacial friction factor is given by the functional form $f_i=a\,Re_c^n$, where [24]

$$f_i=\frac{16}{Re_c}\quad\text{for }0\leqslant Re_c\leqslant 2000, \tag{5a}$$

$$f_i=\frac{0.079}{Re_c^{0.25}}\quad\text{for }2000\leqslant Re_c\leqslant 20{,}000, \tag{5b}$$

$$f_i=\frac{0.046}{Re_c^{0.20}}\quad\text{for }Re_c\geqslant 20{,}000, \tag{5c}$$

and Re_c is the vapor core Reynolds number, defined as

$$Re_c=\frac{\rho_g(\bar{u}_g-u_i)(D_H-2\,\delta)}{\mu_g}. \tag{6}$$

Rearranging terms in Eq. (4) and replacing g by $g\sin\theta$ to allow for orientation angles other than vertical upflow yields

$$\big(\bar{u}_g-u_i\big)^2=\frac{\rho_f\,|g\sin\theta|\,[D_H^2-(D_H-2\,\delta)^2]}{2f_i\,\rho_g(D_H-2\,\delta)}, \tag{7}$$

where $\theta=0$ for horizontal flow and $\theta=90°$ for vertical upflow.

The situation outlined here is one in which the flow is clearly not gravity independent, so it can be safely assumed that the velocity required for gravity independent heat transfer is much greater than that calculated in Eq. (7). This yields the form of the first criterion for gravity independence,

$$\big(\bar{u}_g-u_i\big)^2\gg\frac{\rho_f\,g\,|\sin\theta|\,[D_H^2-(D_H-2\,\delta)^2]}{2f_i\,\rho_g(D_H-2\,\delta)}. \tag{8}$$

For gravity independent cases, where the magnitude of interfacial shear force greatly exceeds that of body force, it is expected that other forces (primarily wall shear force) will increase to balance interfacial shear. Since the goal of the criterion is to establish conditions for which body force is insignificant compared to interfacial shear force, however, information regarding magnitudes of these other forces is not necessary to establish whether the flow is gravity independent.

Recognizing that a characteristic length scale D_F can be defined in Eq. (8) as

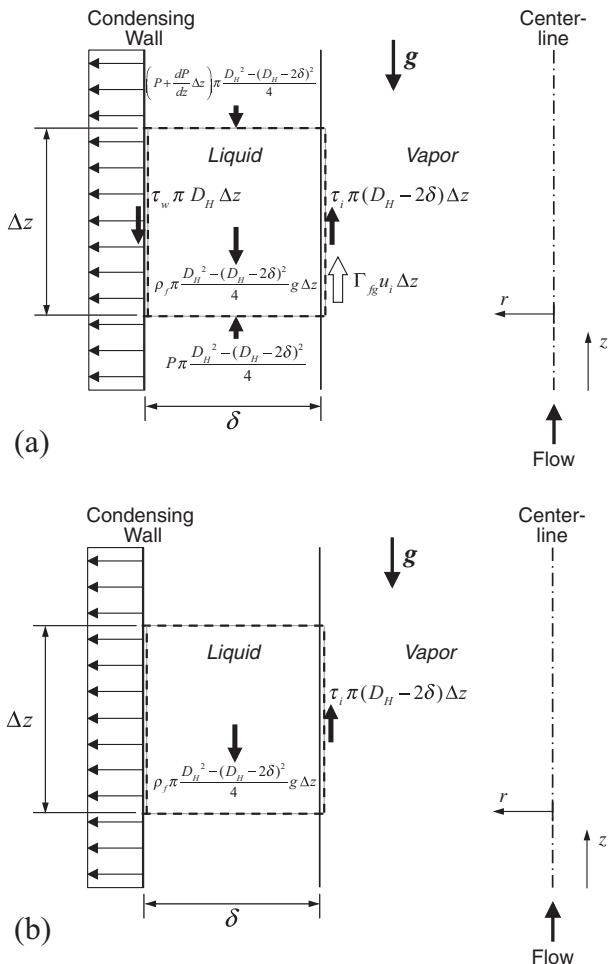$$D_F=\frac{D_H^2-(D_H-2\,\delta)^2}{(D_H-2\,\delta)}, \tag{9}$$

Fig. 4. (a) Force balance for liquid film used to derive first criterion. (b) Simplified force balance for liquid film at onset of flooding.

and rearranging terms to isolate constants, Eq. (8) can be expressed as a combination of dimensionless parameters.

$$2 \gg \frac{1}{|Fr|} \frac{1}{f_i}, \tag{10}$$

where

$$Fr = \frac{\rho_g}{\rho_f} \frac{(\bar{u}_g - u_i)^2}{g \sin \theta D_F} \tag{11}$$

is the Froude number modified by density ratio. Further, implementing the relationship for interfacial friction factor in terms of constants yields the final relationship for the first criterion,

$$|Fr| \gg \frac{1}{2f_i} = \frac{1}{2 a Re_c^n}, \tag{12}$$

where a and n are given by Eqs. (5a)–(5c).

4.2. Component of body force perpendicular to flow direction

For horizontal and near-horizontal orientations, the component of body force acting perpendicular to the interface doesn't directly influence film velocity as the parallel component does, but rather affects the circumferential uniformity of the film, which in turn influences heat transfer performance. In horizontal flow condensation, for inlet conditions where flow inertia is relatively small compared to body force, the liquid tends to pool at the bottom of the channel. As flow inertia increases, however, the film becomes more uniform as the increased interfacial shear stress coupled with surface tension effects act to support a liquid layer above the vapor core. As the establishment of a circumferentially uniform co-current flow regime with comparable velocity magnitudes for every orientation is necessary for a condenser's performance to be gravity independent, it is important to find the exact conditions under which the gravity component perpendicular to flow direction no longer affects the circumferential uniformity of the film.

Fig. 5 shows the relevant parameters for this situation. It is important to note that, counter to the modeling work presented earlier in this study, the interface is no longer considered to be smooth. This is because surface tension effects now play a key role in the ability of the flow to support a liquid layer above the vapor core.

To develop a mechanistic criterion capable of determining the flow conditions at which horizontal flow condensation is able to establish circumferentially uniform annular flow, classic instability

Fig. 5. Linear instability of liquid layer residing above vapor layer used to derive second criterion.

theory will be utilized [37,38]. This theory is based on the assumptions of incompressible and invicid parallel layers of liquid and vapor flowing at of mean velocities $\bar{u}_f$ and $\bar{u}_g$, respectively, and an interfacial perturbation of the form

$$\eta(z,t) = \eta_0 \exp(i k(z - c t)), \tag{13}$$

where η_0 is the amplitude of perturbation, k is the wave number, and c the wave speed. The wave number is related to interfacial wavelength, λ, by the relation $k = 2\pi/\lambda$. Accounting for finite liquid thickness, H_f, and vapor layer thickness, H_g, as outlined by Galloway and Mudawar [39], and replacing g by $g \cos \theta$ to allow for orientation angles other than horizontal yields the following relation for pressure difference generated by interfacial curvature,

$$P_f - P_g = -\left[\rho_f''(c - \bar{u}_f)^2 + \rho_g''(\bar{u}_g - c)^2 + (\rho_f - \rho_g)\frac{g \cos \theta}{k}\right] k\eta, \tag{14}$$

where $\rho_f'' = \rho_f \coth(kH_f)$ and $\rho_g'' = \rho_g \coth(kH_g)$. Pressure difference for a mildly curved interface can be approximated by the product of surface tension and curvature.

$$P_f - P_g \simeq \sigma \frac{\partial^2 \eta}{\partial z^2} = -\sigma k^2 \eta, \tag{15}$$

Equating the pressure difference given by Eqs. (14) and (15) yields the following quadratic equation for wave speed.

$$\rho_f''(c - \bar{u}_f)^2 + \rho_g''(\bar{u}_g - c)^2 + (\rho_f - \rho_g)\frac{g \cos \theta}{k} - \sigma k = 0, \tag{16}$$

which for an unstable interface, yields an expression for c with both real and imaginary components, $c = c_r + i c_i$, where

$$c_r = \frac{\rho_f'' \bar{u}_f + \rho_g'' \bar{u}_g}{\rho_f'' + \rho_g''} \tag{17}$$

and

$$c_i = \sqrt{\frac{\rho_f'' \rho_g'' (\bar{u}_g - \bar{u}_f)^2}{(\rho_f'' + \rho_g'')^2} - \frac{(\rho_f - \rho_g)}{(\rho_f'' + \rho_g'')} \frac{g \cos \theta}{k} - \frac{\sigma k}{\rho_f'' + \rho_g''}}. \tag{18}$$

The interface is rendered unstable when $c_i = 0$, which allows the determination of the critical wavelength, λ_c, corresponding to the onset of instability. A wavelength greater than λ_c would cause peaks in the film along the top wall to grow in an unstable manner and fall across the vapor core. Therefore, λ_c is the upper limit for interfacial wavelength that would maintain the top film intact. Setting $c_i = 0$ in Eq. (18) yields

$$k_c = \frac{2\pi}{\lambda_c} = \frac{\rho_f'' \rho_g'' (\bar{u}_g - \bar{u}_f)^2}{2\sigma(\rho_f'' + \rho_g'')} \left\{ 1 + \sqrt{1 + 4 \frac{(\rho_f - \rho_g)(\rho_f'' + \rho_g'')^2 \sigma g \cos \theta}{\rho_f''^2 \rho_g''^2 (\bar{u}_g - \bar{u}_f)^4}} \right\}. \tag{19}$$

Notice in Eq. (19) that the effect of gravity is contained in the second term under the radical. It may therefore be inferred that the flow becomes independent of gravity when this term approaches zero, which yields the second criterion for gravity independence corresponding to the component of gravity perpendicular to the flow direction.

$$\frac{(\rho_f - \rho_g)(\rho_f'' + \rho_g'')^2 \sigma |g \cos \theta|}{\rho_f''^2 \rho_g''^2 (\bar{u}_g - \bar{u}_f)^4} \ll \frac{1}{4}. \tag{20}$$

This approach is very reminiscent of the criterion developed by Zhang et al. [15] to negate the influence of component of gravity perpendicular to the flow direction on flow boiling CHF.
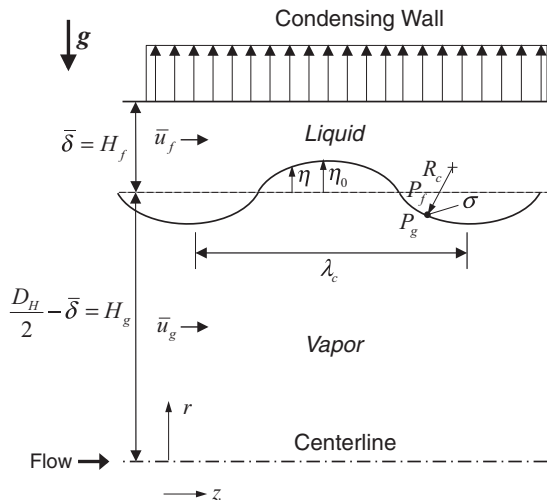
Defining Bond and Weber numbers as

$$Bo = \frac{(\rho_f - \rho_g)\, g\, \cos\theta L_{char}^2}{\sigma} \qquad (21)$$

and

$$We = \frac{(\rho_f'' \rho_g'')\, (\bar{u}_g - \bar{u}_f)^2 L_{char}}{(\rho_f'' + \rho_g'')\sigma}, \qquad (22)$$

respectively, with a characteristic length L_{char} that will cancel out, Eq. (20) can be rewritten as

$$\frac{|Bo|}{We^2} \ll \frac{1}{4}. \qquad (23)$$

5. Evaluation of criteria

In order to move forward and begin utilizing the criteria given by Eqs. (12) and (23), it is first necessary to establish a combination of operating conditions for which flow condensation heat transfer has been experimentally determined to be independent of gravity. Fig. 6(a) shows heat transfer coefficient averaged over the two-phase region of the condensation length (i.e., not including the short upstream superheated portion) plotted against FC-72 mass velocity. It is clear that at low mass velocities the heat transfer coefficient is highest for vertical downflow and lowest for vertical upflow, with values for horizontal falling in between. As explained earlier, this is due to the role of body force in aiding liquid film motion for vertical downflow and retarding it for vertical upflow. As mass velocity is increased, the three heat transfer coefficient values begin to converge together, with the highest mass velocities tested exhibiting almost no difference in heat transfer coefficient among the three orientations. Fig. 6(b) reinforces this trend by plotting the ratios of average heat transfer coefficients for both vertical upflow and downflow to those for horizontal flow versus G_{FC}/ρ_f. Viewing these two figures together, it is clear that the mass velocity at which convergence of heat transfer coefficients occurs is $G_{crit} = 424$ kg/m^2 s.

Notice that the characteristic velocities $(\bar{u}_g - u_i)$ and $(\bar{u}_g - \bar{u}_f)$ used in the first criterion, Eq. (12), and second criterion, Eq. (23), respectively, are not known a priori. However, an approximate characteristic velocity difference ΔU_{char} composed of mean outlet vapor and liquid velocities of the form

$$\bar{u}_g - u_i \approx \bar{u}_g - \bar{u}_f = \frac{G_{g,out}}{\rho_g \alpha_{out}} - \frac{G_{f,out}}{\rho_f(1 - \alpha_{out})} = \Delta U_{char}, \qquad (24)$$

where $G_{g,out} = G_{FC} x_{e,out}$ and $G_{f,out} = G_{FC}(1 - x_{e,out})$, can be used. As mentioned earlier, the use of exit values when evaluating the criteria is crucial, as liquid mass accumulation along the condensing length means both criteria become most difficult to satisfy at the channel exit.

Exit quality $x_{e,out}$ is used to calculate void fraction at the outlet using Zivi's relation for void fraction [40],

$$\alpha_{out} = \left[1 + \left(\frac{1 - x_{e,out}}{x_{e,out}} \right)\left(\frac{\rho_g}{\rho_f} \right)^{2/3} \right]^{-1}. \qquad (25)$$

This void fraction value is then used to determine film thickness at the exit, δ_{out}, where $\alpha_{out} = (D_H - 2\delta_{out})^2/D_H^2$. The value of δ_{out} is substituted into Eq. (9) to calculate the characteristic length scale D_F used in the definition of Fr, used directly in the calculation of vapor core Reynolds number Re_c according to Eqs. (5a)–(5c), and substituted into the expressions $H_f = \delta_{out}$ and $H_g = D_H - \delta_{out}$ in ρ_f'' and ρ_g'', respectively. All fluid properties are determined from FC-72 saturation properties based on exit pressure.
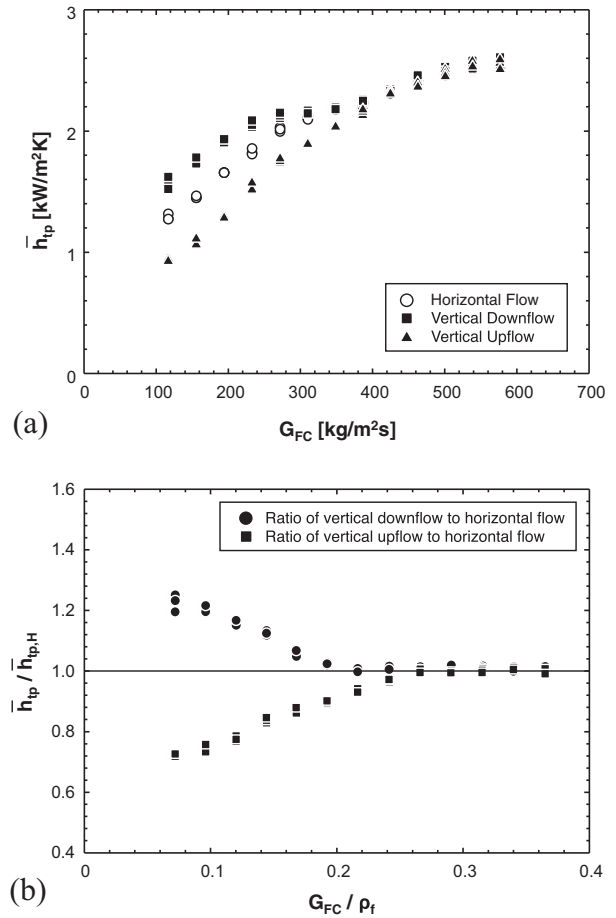

(a)

(b)

Fig. 6. (a) Comparison of experimentally-determined condensation heat transfer coefficients averaged over two-phase region with FC-72 mass velocity for three flow orientations. (b) Variations of heat transfer coefficient averaged over two-phase region with G_{FC}/ρ_f, with heat transfer coefficients for vertical upflow and vertical downflow normalized relative to those for horizontal flow.

After finding interfacial friction factor using Re_c according to Eqs. (5a)–(5c), all unknowns in the first criterion, Eq. (12), can be eliminated. For the second criterion, it is still necessary to calculate the critical wavenumber k_c using Eq. (19) in order to determine the modified densities ρ_f'' and ρ_g''. Use of Eq. (24) as the characteristic velocity difference provides values for critical wavelength up to $\lambda_c = 1$ mm, which are somewhat lower than those presented in the first part of the present study [21]. This is due to the fact that the mass velocities used to measure wavelengths in the first part were $G_{FC} = 39.94$ and 79.78 kg/m^2 s, while the mass velocities investigated here fall in the much higher range of $G_{FC} = 116.75$–576.56 kg/m^2 s.

After finding k_c, all unknown quantities in the second criterion are determined, and both criteria may be evaluated. Table 2 outlines the step-by-step procedures and equations used to calculate values for both criteria using the method outlined above.

Using this method, critical conditions for negating gravity effects according to both criteria can be found for the experimental operating conditions where the onset of gravity independence is found to occur as shown in Fig. 6(a) and (b). This corresponds to $G_{FC} = 424.3$ and 424.4 kg/m^2, $x_{e,out} = 0.46$ and 0.49, and $P_{out} = 151.6$ and 145.1 kPa, for the critical cases for vertical upflow and corresponding horizontal flow conditions, respectively. Using these values, the criteria for gravity independence can be defined as

Table 2
Procedure for evaluating criteria using simplified characteristic velocity.

Step no.		Equation(s)
First criterion		
1.	Determine exit quality, $x_{e,out}$, to account for heat lost by condensation	
2.	Evaluate fluid properties using exit pressure	
3.	Use Zivi correlation [40] to calculate exit void fraction α_{out}	$\alpha_{out} = \left[1 + \left(\frac{1-x_{e,out}}{x_{e,out}}\right)\left(\frac{\rho_g}{\rho_f}\right)^{2/3}\right]^{-1}$
4.	Use void fraction to calculate exit film thickness δ_{out}	$\alpha_{out} = (D_H - 2\delta_{out})^2 / D_H^2$
5.	Define characteristic velocity U_{char}	$U_{char} = \bar{u}_g - u_i = \left[\frac{G_{FC}x_{e,out}}{\rho_g \alpha_{out}} - \frac{G_{FC}(1-x_{e,out})}{\rho_f(1-\alpha_{out})}\right]$
6.	Calculate vapor core Reynolds number Re_c	$Re_c = \frac{\rho_g U_{char}(D_H - 2\delta_{out})}{\mu_g}$
7.	Use Re_c to calculate interfacial friction factor f_i	$f_i = \frac{16}{Re_c}$ for $0 \leqslant Re_c \leqslant 2000$ $f_i = \frac{0.079}{Re_c^{0.25}}$ for $2000 \leqslant Re_c \leqslant 20,000$ $f_i = \frac{0.046}{Re_c^{0.20}}$ for $Re_c \geqslant 20,000$
8.	Use first criterion to determine if given configuration (inlet conditions, geometry, orientation, wall heat flux profile) can achieve gravity independence	$D_F = \frac{D_H^2 - (D_H - 2\delta_{out})^2}{(D_H - 2\delta_{out})}$ $|Fr| = \frac{\rho_g}{\rho_f} \frac{U_{char}^2}{|g\sin\theta|D_F} > \frac{0.235}{f_i}$
Second criterion		
1.	Determine exit quality, $x_{e,out}$, to account for heat lost by condensation	
2.	Evaluate fluid properties using exit pressure	
3.	Use Zivi correlation [40] to calculate exit void fraction α_{out}	$\alpha_{out} = \left[1 + \left(\frac{1-x_{e,out}}{x_{e,out}}\right)\left(\frac{\rho_g}{\rho_f}\right)^{2/3}\right]^{-1}$
4.	Use void fraction to calculate exit film thickness δ_{out}	$\alpha_{out} = (D_H - 2\delta_{out})^2 / D_H^2$
5.	Define characteristic velocity U_{char}	$U_{char} = \bar{u}_g - u_i = \left[\frac{G_{FC}x_{e,out}}{\rho_g \alpha_{out}} - \frac{G_{FC}(1-x_{e,out})}{\rho_f(1-\alpha_{out})}\right]$
6.	Solve Eq. (18) iteratively for critical wavenumber k_c	$k_c = \frac{2\pi}{\lambda_c} = \frac{\rho_f'' \rho_g'' U_{char}^2}{2\sigma(\rho_f'' + \rho_g'')}\left\{1 + \sqrt{1 + 4\frac{(\rho_f - \rho_g)(\rho_f'' + \rho_g'')^2\sigma g\cos\theta}{\rho_f''^2 \rho_g''^2 U_{char}^4}}\right\}$ $\rho_f'' = \rho_f \coth(k_c H_f)$ $\rho_g'' = \rho_g \coth(k_c H_g)$
7.	Evaluate ρ_f'' and ρ_{gv}'' using the calculated critical wavenumber	$\rho_f'' = \rho_f \coth(k_c H_f)$ $\rho_g'' = \rho_g \coth(k_c H_g)$
8.	Use second criterion to determine if given configuration (inlet conditions, geometry, orientation, wall heat flux profile) can achieve gravity independence	$\frac{|Bo|}{We^2} = \frac{(\rho_f - \rho_g)(\rho_f'' + \rho_g'')^2 \sigma|g\cos\theta|}{\rho_f''^2 \rho_g''^2 U_{char}^4} < 5.12 \times 10^{-5}$

$$|Fr| > \frac{0.235}{a\,Re_c^n} \qquad (26)$$

and

$$\frac{|Bo|}{We^2} < 5.12 \times 10^{-5}. \qquad (27)$$

The fact that Eq. (26) exceeds the inequality established in Eq. (12) may be attributed to the neglected force terms in the derivation of the first criterion, and does not affect the validity of Eq. (26) as a tool to predict gravity independence.

5.1. Parametric trends

Now that the two criteria have been explicitly defined, different cases can be evaluated to determine how the constants in the criteria change with respect to different input parameters. Fig. 7(a) shows values for the first criterion (associated with the component of body force parallel to the flow direction), plotted versus angle of orientation, θ. All cases are evaluated for constant outlet pressure and quality to isolate trends relative to only angle of orientation and mass velocity. It is clear that the criterion becomes hardest to satisfy at $\theta = \pm 90°$ (vertical upflow and vertical downflow), where the magnitude of body force in the flow direction is at its maximum. It is also clear that the criterion values are at their maximum for the lowest mass velocities, and decrease with increasing mass velocity. This is closely associated with the trend of interfacial shear stress increasing in magnitude with increasing mass velocity, and eventually dominating body force for the highest mass velocities, implying that the criterion is satisfied. Fig. 7(b) shows three of the highest inlet mass velocity cases tested, with

the increased influence of interfacial shear stress clearly manifest in the significantly smaller vertical axis values compared to those in Fig. 7(a).

Similarly, Fig. 7(c) shows values for the second criterion (associated with the component of body force perpendicular to the flow direction) plotted versus angle of orientation, θ. It is clear this criterion becomes hardest to satisfy at orientations near $\theta = 0°$ and 180°, where the component of gravity perpendicular to the interface reaches its maximum. Again, the criterion values exhibit maximum amplitude for the lowest mass velocities, and decrease with increasing mass velocity, signifying that flow inertia is increasingly capable of balancing body force. Fig. 7(d) shows three of the highest inlet mass velocity cases tested, with their values greatly reduced compared to those shown in Fig. 7(c).

Fig. 8(a)–(c) shows the inlet mass velocity required to ensure gravity independence as a function of local gravitational acceleration for exit qualities of $x_{e,out} = 0.5$ (close to experimental value used to derive criteria), 0.15, and 0.85, respectively, again using a constant outlet pressure. The required inlet mass velocity is found by replacing the inequalities in Eqs. (26) and (27) with equal signs and iterating through the procedure in Table 2 (changing mass velocity) until the equation is satisfied. It is important to note that the local acceleration values provided on the horizontal axis of these plots can represent a varying angle of orientation in a constant acceleration environment, a constant angle of orientation in a varying acceleration environment, or a combination of the two. Earth, Martian, and Lunar gravitational accelerations are marked to provide a reference for interpretation of the trends.

Fig. 8(a) shows that, for an intermediate exit quality of $x_{e,out} = 0.5$, the component of body force perpendicular to the flow direction is the limiting factor for gravity independence for accel-
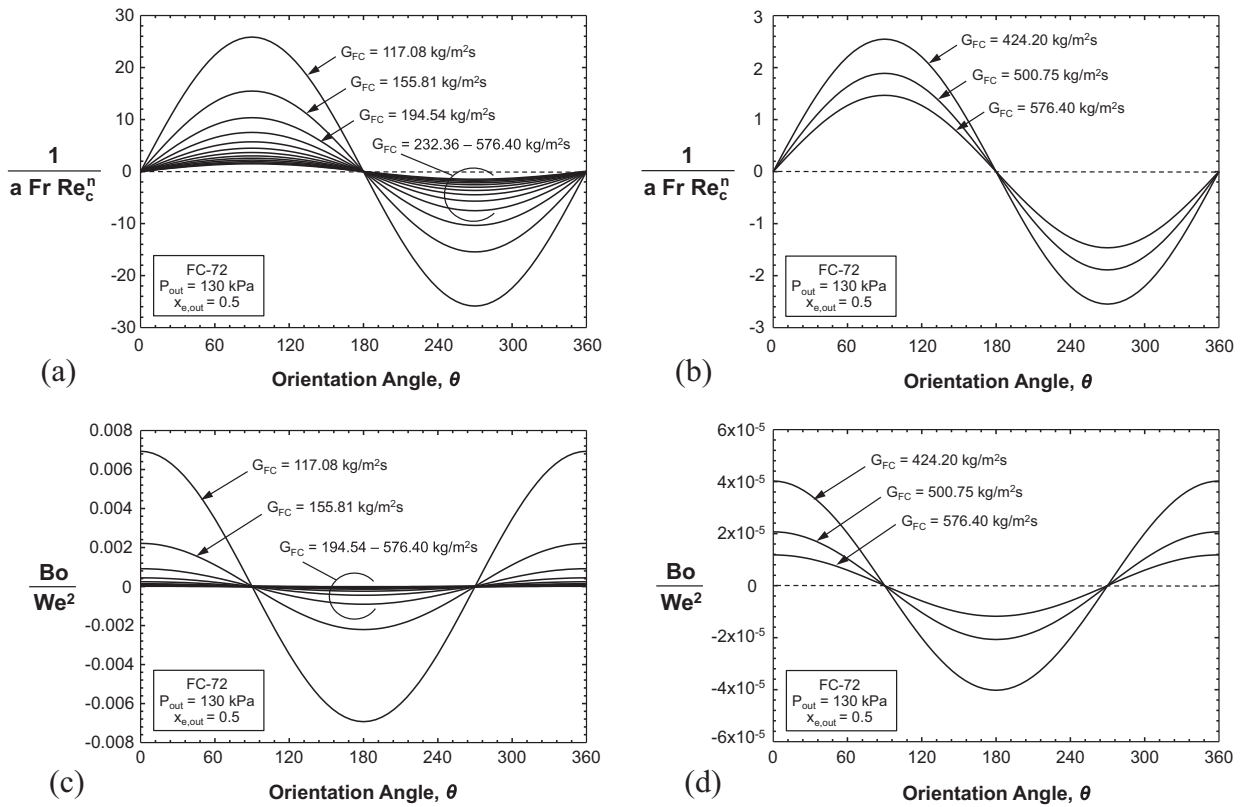
Fig. 7. (a) Values of dimensionless group in first criterion versus orientation angle, evaluated for all experimental mass velocities. (b) Values of dimensionless group in first criterion versus orientation angle, evaluated for highest three mass velocities. (c) Values of dimensionless group in second criterion versus orientation angle, evaluated for all experimental mass velocities. (d) Values of dimensionless group in second criterion versus orientation angle, evaluated for highest three mass velocities.

erations ranging from zero to about 20 m/s², which encompasses Lunar, Martian and Earth gravitational accelerations. Above this acceleration value, the component of body force parallel to the flow direction becomes the limiting factor in attaining gravity independence. This latter range would include, for example, a two-phase thermal management system employed in a military aircraft undergoing high gravity maneuvers.

Fig. 8(b) shows that as exit quality is decreased to $x_{e,out}$ = 0.15 (indicating a higher percentage of vapor is condensed to liquid before exiting the channel), the component of body force parallel to the flow direction (first criterion) dominates over a much larger range of accelerations, including Lunar, Martian and Earth gravitational accelerations, compared to $x_{e,out}$ = 0.15, Fig. 8(a). This makes physical sense, as flooding is strongly dependent on liquid mass, while interfacial stability is only weakly so.

Similarly, Fig. 8(c) shows that as exit quality is increased to $x_{e,out}$ = 0.85 (indicating a lower percentage of vapor is condensed to liquid before exiting the channel), the component of body force perpendicular to the interface dominates for most relevant gravitational accelerations, while the component of body force parallel to the flow direction becomes the limiting factor only for extremely high accelerations.

Care should be taken when using the second criterion to evaluate cases with exit quality below $x_{e,out}$ = 0.15. The hyperbolic cotangent terms present within the modified densities in Eq. (23) account for the influence of exit quality by making the criterion harder to satisfy as exit quality decreases from $x_{e,out}$ = 1.0 to 0.15, but for $x_{e,out}$ < 0.15 it predicts that interfacial stability is easier to achieve. This is due to the behavior of hyperbolic cotangent near input values of zero.

In addition to concerns regarding the hyperbolic cotangent terms, care should be taken when evaluating both criteria at qual-

ities lower than $x_{e,out}$ = 0.15 due to the probability of the flow transitioning out of annular flow (for which the criteria were developed) into other flow regimes, such as slug, plug, or bubbly flow, which exhibit drastically different interfacial characteristics and are driven less by interfacial shear than annular flow and more by other forces. The heat transfer characteristics of these lower void fraction regimes are less susceptible to body force effects, however, as they are far less separated than annular flow, meaning that, if the flow is gravity independent up to $x_{e,out}$ = 0.15, it is likely to continue to be so for even lower $x_{e,out}$ values, including full condensation.

5.2. Evaluation of experimental results

Having established critical values for the criteria, the experimental results gathered previously can be evaluated to determine which cases satisfy the gravity independence criteria.

Fig. 9(a) shows values of the dimensionless group in the first criterion (governing the influence of body force parallel to the flow direction), evaluated for the cases of vertical upflow and downflow, and plotted versus their respective mass velocities. In this plot, experimental exit quality is used for each case, along with FC-72 fluid properties evaluated at the experimentally measured exit pressure. Points below the horizontal dashed line indicate that the configuration's heat transfer performance would be independent of gravity, which can be verified by Fig. 6. Overall, the first criterion is shown predicting the mass velocity corresponding to gravity independence fairly well for both orientations and most of the data.

Fig. 9(b) shows values of the dimensionless group in the second criterion (governing the influence of body force perpendicular to the flow direction), evaluated for the case of horizontal flow, and
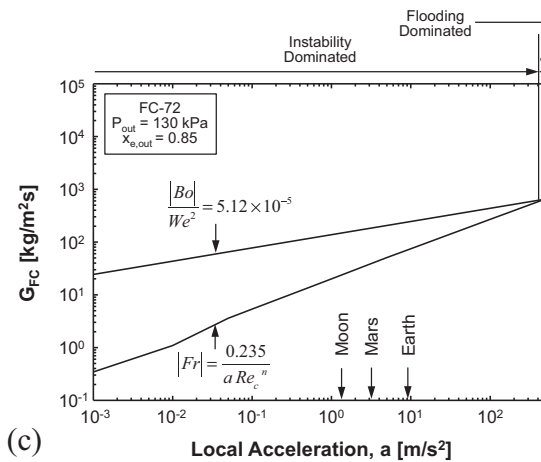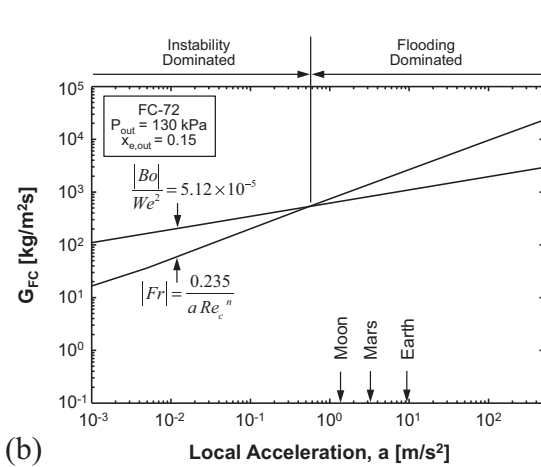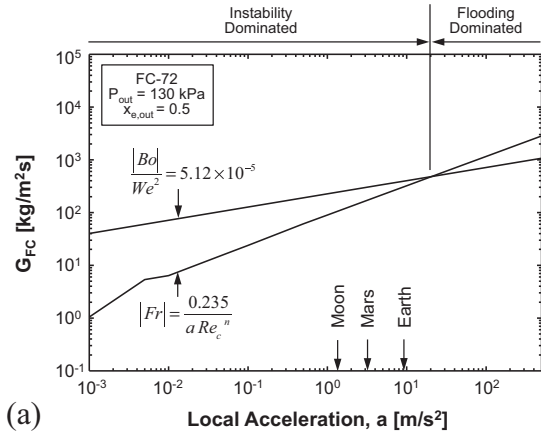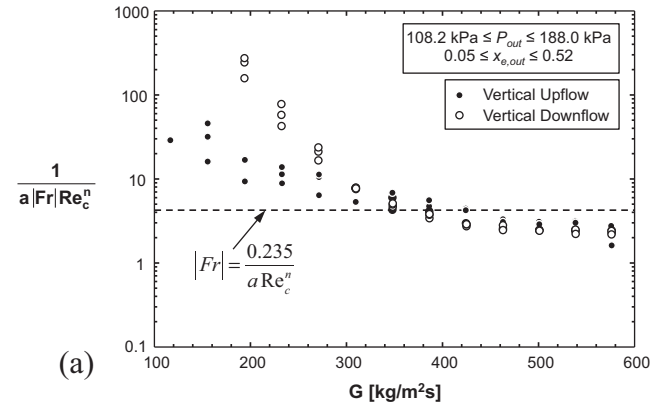
Fig. 8. Mass velocity required to achieve gravity independence versus local acceleration for (a) $x_{e,out}$ = 0.5, (b) $x_{e,out}$ = 0.15, and (c) $x_{e,out}$ = 0.85.

Fig. 9. (a) Values of dimensionless group in first criterion versus inlet mass velocity, evaluated using experimental exit conditions. (b) Values of dimensionless group in second criterion versus inlet mass velocity, evaluated using experimental exit conditions.
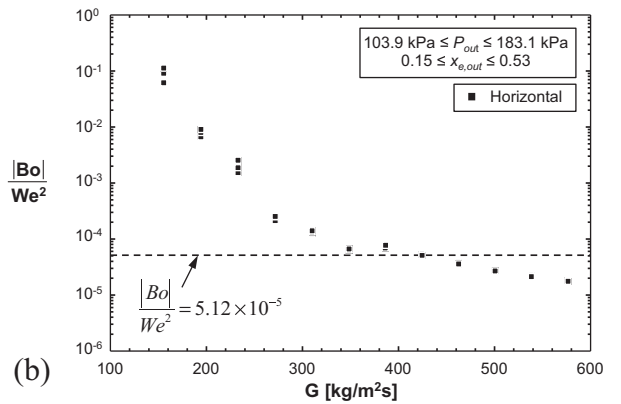
plotted versus mass velocities. Values are seen to decrease monotonically with increasing mass velocity, with the criterion predicting the mass velocity corresponding to gravity independence with reasonable accuracy.

5.3. Use of separated flow model to predict gravity independence

Thus far, evaluations of both criteria have utilized Eq. (24) as characteristic velocity, as experimental measurements of film, core, and interfacial velocities are not available. In their original formulations, however, the first and second criterion depend on $\bar{u}_g - u_i$ and $\bar{u}_g - \bar{u}_f$ as characteristic velocities, respectively, both

of which can be calculated at the channel exit more systematically through use of the separated flow model outlined in Table 1. Exit film thickness δ_{out} is also calculated by the separated flow model without having to rely on the Zivi correlation [40]. Table 3 outlines the procedure and equations used to evaluate the gravity independence criteria using information provided by the Separated Flow Model. Additionally, use of the separated flow model has the added benefit of coupling the calculation of film and vapor velocities with the channel's orientation, rather than orientation simply being input independent of the characteristic velocity used. This serves to heighten its accuracy as a tool to predict gravity independence when coupled with the dimensionless criteria derived earlier.

Before utilizing the criteria with separated flow model predictions, however, critical values of the two dimensionless groups must be revaluated using the values of film, vapor, and interfacial velocities determined by the separated flow model for the case of G_{crit} = 424.4 kg/m² s for both vertical upflow and horizontal flow. Doing this yields the following revised criteria,

$$|Fr| > \frac{0.195}{a\,Re_c^n} \qquad (28)$$

and

$$\frac{|Bo|}{We^2} < 2.32 \times 10^{-5}. \qquad (29)$$

Notice how the new constant for the first criterion, 0.195, is slightly smaller than in Eq. (26), 0.235, that was derived using the simplified characteristic velocity. However, the constant in the second criterion, 2.32×10^{-5}, is less than half that in Eq. (27), 5.12×10^{-5}, using the simplified characteristic velocity.

Table 3
Procedure for evaluating criteria using Separated Flow Model results.

Step no.		Equation(s)
First criterion		
1.	Use experimental inlet pressure and mass velocity to run Separated Flow Model (SFM) for the given channel geometry, orientation and wall heat flux distribution, and determine δ_{out}, u_g, u_f, and u_i at the channel exit	See Table 1
2.	Evaluate fluid properties using exit pressure	
3.	Calculate vapor core Reynolds number Re_c	$Re_c = \frac{\rho_g\left(\bar{u}_g - u_i\right)(D_H - 2\delta_{out})}{\mu_g}$
4.	Use Re_c to calculate interfacial friction factor f_i	$f_i = \frac{16}{Re_c}$ for $0 \leqslant Re_c \leqslant 2000$ $f_i = \frac{0.079}{Re_c^{0.25}}$ for $2000 \leqslant Re_c \leqslant 20,000$ $f_i = \frac{0.046}{Re_c^{0.20}}$ for $Re_c \geqslant 20,000$
5.	Use first criterion to determine if given configuration (inlet conditions, geometry, orientation, wall heat flux profile) can achieve gravity independence	$D_F = \frac{D_H^2 - (D_H - 2\delta_{out})^2}{(D_H - 2\delta_{out})}$ $|Fr| = \frac{\rho_g}{\rho_f}\frac{\left(\bar{u}_g - u_i\right)^2}{|g\sin\theta|D_F} > \frac{0.195}{f_i}$
Second criterion		
1.	Use experimental inlet pressure and mass velocity to run Separated Flow Model (SFM) for the given channel geometry, orientation and wall heat flux distribution, and determine δ_{out}, u_g, u_f, and u_i at the channel exit	See Table 1
2.	Evaluate fluid properties using exit pressure	
3.	Solve Eq. (18) iteratively for critical wavenumber k_c	$k_c = \frac{2\pi}{\lambda_c} = \frac{\rho_f'' \rho_g'' U_{char}^2}{2\sigma(\rho_f'' + \rho_g'')}\left\{1 + \sqrt{1 + 4\frac{(\rho_f - \rho_g)(\rho_f'' + \rho_g'')^2 \sigma\cos\theta}{\rho_f''^2 \rho_g''^2 U_{char}^4}}\right\}$ $\rho_f'' = \rho_f \coth(k_c H_f)$ $\rho_g'' = \rho_g \coth(k_c H_g)$ $\rho_f'' = \rho_f \coth(k_c H_f)$ $\rho_g'' = \rho_g \coth(k_c H_g)$
4.	Evaluate ρ_f'' and ρ_{gv}'' using the calculated critical wavenumber	
5.	Use second criterion to determine if given configuration (inlet conditions, geometry, orientation, wall heat flux profile) can achieve gravity independence	$\frac{|Bo|}{We^2} = \frac{(\rho_f - \rho_g)(\rho_f'' + \rho_g'')^2 \sigma|g\cos\theta|}{\rho_f''^2 \rho_g''^2 U_{char}^4} < 2.32 \times 10^{-5}$

To illustrate the enhanced fidelity provided by using inputs from the separated flow model, the model is run for inlet conditions associated with the prior experiments, as well as hypothetical cases of $\theta = 45°$ (or 135° because of test section symmetry) and $\theta = 225°$ (315°) using inlet conditions averaged between those of vertical upflow and horizontal, and vertical downflow and horizontal, respectively.

Fig. 10(a) shows values of the dimensionless group in the first criterion plotted versus angle of orientation. Similar to Fig. 7 (a) and (b), the value approaches zero for orientations near horizontal. Due to its advantageous coupling of orientation with velocity calculation, however, the separated flow model results show significant differences between values for upflow and downflow configurations. For the intermediate orientations of $\theta = 135°$ (45°) and 225° (315°) the values are closer in magnitude, with the difference between the two orientations decreasing with increasing mass velocity. This makes physical sense, as gravity assists liquid film motion in vertical downflow while hinders it in vertical upflow.

Fig. 10(b) shows values of the dimensionless group in the second criterion plotted versus angle of orientation for the same orientations as in Fig. 10(a). Similar to Fig. 7(c) and (d), the value approaches zero for orientations near vertical. Compared to Fig. 7 (c) and (d), however, Fig. 10(b) exhibits significant asymmetry. The dimensionless group achieves peak value somewhere between horizontal and $\theta = 225°$ rather than for perfectly horizontal orientations. This can be explained by considering that at $\theta = 180°$ there is no component of gravity acting in the direction of fluid motion, and the liquid film velocity is entirely dependent on the vapor core velocity. As the angle of orientation moves away from horizontal, the component of gravity acting perpendicular to the interface is diminished, but a component of gravity acting parallel to the flow direction is established. This component acts to increase liquid film velocity for $\theta = 225°$, which in turn reduces the value of $\left(\bar{u}_g - \bar{u}_f\right)^4$. This velocity difference is present in the denominator of the second
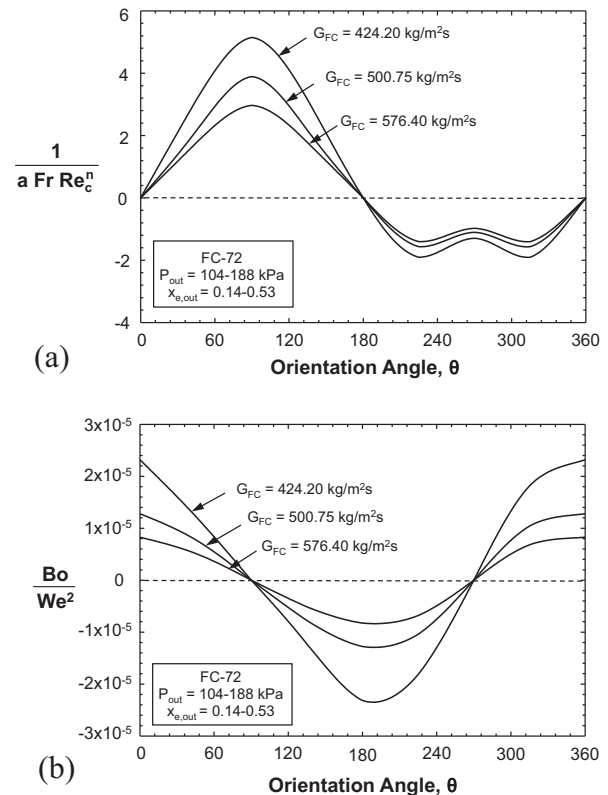

(a)

(b)

Fig. 10. (a) Values of dimensionless group in first criterion, evaluated using separated flow model results, versus orientation angle for different mass velocities. (b) Values of dimensionless group in second criterion, evaluated using separated flow model results, versus orientation angle for different mass velocities. All separated flow model calculations are based on identical inlet quality of $x_{e,in} = 1.0$.
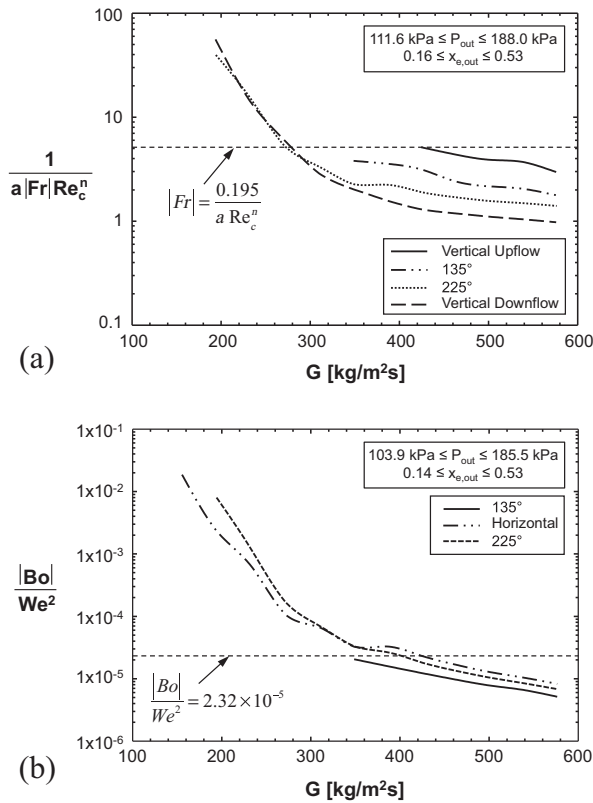
Fig. 11. (a) Values of dimensionless group in first criterion, evaluated using separated flow model and experimental exit conditions, versus inlet mass velocity for different orientations. (b) Values of dimensionless group in second criterion, evaluated using separated flow model and experimental exit conditions versus inlet mass velocity for different orientations. All separated flow model calculations are based on identical inlet quality of $x_{e,in}$ = 1.0.

criterion, Eq. (23), and, because of its large exponent, the ability of a given flow configuration to mitigate the effects of body force perpendicular to the interface is strongly dependent on it.

Fig. 11(a) shows values of the dimensionless group in the first criterion, again determined using film thickness, film velocity, vapor velocity, and interfacial velocities at the exit of the channel calculated by the separated flow model, plotted versus inlet mass velocity. Similar to the trend displayed in Fig. 10(a), by coupling velocity determination with angle of orientation, significant differences between vertical upflow and vertical downflow orientations are seen. It can be clearly seen in Fig. 11(a) that vertical downflow and θ = 225° orientations first satisfy the critical value at inlet mass velocities of approximately G_{FC} = 280 kg/m² s, while vertical upflow is unable to satisfy the criterion until G_{FC} = 425 kg/m² s. The transition point for θ = 135° could not be calculated because the separated flow model does not converge at this orientation for lower mass velocities.

Fig. 11(b) shows values of the dimensionless group in the second criterion plotted versus inlet mass velocity. Similar to Fig. 11(a), the transition point for θ = 135° could not be determined, but it is clear that the dimensionless group is first able to satisfy the criteria for this orientation, having already achieved gravity independence at a relatively low mass velocity of G_{FC} = 348.54 kg/m² s. Horizontal and θ = 225° orientations require higher mass velocities to achieve gravity independence, as horizontal flow is associated with maximum value of body force perpendicular to the interface, and θ = 225° trades a reduced component of body

force perpendicular to the interface for a reduced velocity difference due to the component of body force parallel to flow direction assisting liquid film motion.

Based on a comparison of results found using Eq. (24) as characteristic velocity to those generated using values $\bar{u}_g - u_i$ and $\bar{u}_g - \bar{u}_f$ output by the separated flow model, it is clear that utilization of the separated flow model provides higher fidelity predictions capable of capturing relevant physical trends missed by the first approach. For this reason, it is recommended that simulations using the separated flow model be performed and the relevant parameters used in the criteria defined in Eqs. (28) and (29) when attempting to predict whether a given condenser's performance will be independent of gravity.

Lastly, as discussed in the first part of the study [21], future studies addressing the effects of gravity on annular flow condensation must rely on better mechanistic modeling of the transport behavior of the annular liquid film. Such modeling would benefit greatly from the use of more sophisticated diagnostic tools to measure detailed temporal records and statistical averaging of film thickness and wave propagation, as well as velocity and temperature profiles across the film. The reader should refer to Refs. [29,41–47] for more detailed information concerning these diagnostic tools.

6. Conclusions

This study investigated the complex interactions between fluid inertia and body force in flow condensation at different orientations. A control-volume based separated flow model was solved numerically to determine the relative magnitude of forces acting on the liquid film in annular flow condensation. The outcomes from the force term comparison were used to develop a pair of mechanistic criteria, expressed in terms of relevant dimensionless groups, capable of predicting the mass velocity required for gravity independent flow condensation heat transfer. Experimental heat transfer results were presented that exhibit a clear transition to gravity independence, which was utilized to explicitly determine dimensionless group values for which gravity independence is achieved. Key findings from the study are as follows:

1. Use of the separated flow model to compare the relative magnitude of different forces acting on the liquid film shows that the contribution of pressure gradient and momentum transfer due to phase change across the interface are negligible for the range of operating conditions evaluated here. Body force (gravity) has a significant contribution relative to that of wall and interfacial shear forces for low mass velocities. As mass velocity increases, the contribution of body force decreases, while that of interfacial shear force increases.

2. Two dimensionless criteria were developed to determine the minimum mass velocity required to overcome body force effects on flow condensation heat transfer. The criteria trends were evaluated relative to variations in mass velocity, angle of orientation, local gravitational acceleration, and exit quality, as well directly evaluating experimental results. The criteria were shown to exhibit physically sound trends for broad ranges of these parameters.

3. Use of the separated flow model alongside the gravity independence criteria was presented as a potential design tool for engineers seeking to determine whether a given condenser would perform independent of its orientation in a local acceleration field. Cases evaluated here indicate the methodology is sound, and its use allows for the capture of relevant physical trends. However, due to the relatively small number of data points used

    L.E. O'Neill et al./International Journal of Heat and Mass Transfer 106 (2017) 313–328

for analysis, future studies involving a broader range of working fluids and operating environments are necessary to fully validate the criteria and methodology presented here.

Acknowledgements

References

[1] I. Mudawar, Two-phase micro-channel heat sinks: theory, applications, and limitations, J. Electron. Pack. – Trans. ASME 133 (2011) 041002.

[2] T.M. Anderson, I. Mudawar, Microelectronic cooling by enhanced pool boiling of a dielectric fluorocarbon liquid, J. Heat Transfer Trans. ASME 111 (1989) 752–759.

[3] D.D. Hall, I. Mudawar, Ultra-high critical heat flux (CHF) for subcooled water flow boiling – II. High-CHF database and design parameters, Int. J. Heat Mass Transfer 42 (1999) 1429–1456.

[4] S. Mukherjee, I. Mudawar, Smart pumpless loop for micro-channel electronic cooling using flat and enhanced surfaces, IEEE Trans. – CPMT: Comp. Pack. Technol. 26 (2003) 99–109.

[5] S. Mukherjee, I. Mudawar, Pumpless loop for narrow channel and micro-channel boiling from vertical surfaces, J. Electron. Pack. – Trans. ASME 125 (2003) 431–441.

[6] Y. Katto, M. Kunihiro, Study of the mechanism of burn-out in boiling system of high burn-out heat flux, Bullet. JSME 16 (1973) 1357–1366.

[7] M.E. Johns, I. Mudawar, An ultra-high power two-phase jet-impingement avionic clamshell module, J. Electron. Pack. – Trans. ASME 118 (1996) 264–270.

[8] L. Lin, R. Ponnappan, Heat transfer characteristics of spray cooling in a closed loop, Int. J. Heat Mass Transfer 46 (2003) 3737–3746.

[9] M. Visaria, I. Mudawar, Theoretical and experimental study of the effects of spray inclination on two-phase spray cooling and critical heat flux, Int. J. Heat Mass Transfer 51 (2008) 2398–2410.

[10] I. Mudawar, D. Bharathan, K. Kelly, S. Narumanchi, Two-phase spray cooling of hybrid vehicle electronics, IEEE Trans. – CPMT: Comp. Pack. Technol. 32 (2009) 501–512.

[11] J.R. Thome, Condensation in plain horizontal tubes: recent advances in modelling of heat transfer to pure fluids and mixtures, J. Brazil. Soc. Mech. Sci. Eng. 27 (2005) 23–30.

[12] H. Lee, I. Mudawar, M.M. Hasan, Flow condensation in horizontal tubes, Int. J. Heat Mass Transfer 66 (2013) 31–45.

[13] S.M. Kim, I. Mudawar, Theoretical model for local heat transfer coefficient for annular flow boiling in circular mini/micro-channels, Int. J. Heat Mass Transfer 73 (2014) 731–742.

[14] S.M. Kim, J. Kim, I. Mudawar, Flow condensation in parallel micro-channels – part 1: experimental results and assessment of pressure drop correlations, Int. J. Heat Mass Transfer 55 (2012) 971–983.

[15] H. Zhang, I. Mudawar, M.M. Hasan, A method for assessing the importance of body force on flow boiling CHF, J. Heat Transfer – Trans. ASME 126 (2004) 161–168.

[16] C. Konishi, I. Mudawar, M.M. Hasan, Criteria for negating the influence of gravity on flow boiling critical heat flux with two-phase inlet conditions, Int. J. Heat Mass Transfer 65 (2013) 203–218.

[17] J.C. Chato, Laminar Condensation Inside Horizontal and Inclined Tubes, Doctoral dissertation, Massachusetts Institute of Technology, Cambridge, Massachusetts, 1960.

[18] S. Lips, J.P. Meyer, Effect of gravity forces on heat transfer and pressure drop during condensation of R134a, Micrograv. Sci. Technol. 24 (2012) 157–164.

[19] H. Lee, I. Park, C. Konishi, I. Mudawar, R.I. May, J.R. Juergend, J.D. Wagner, N.R. Hall, H.K. Nahra, M.M. Hasan, J.R. Mackey, Experimental investigation of flow condensation in microgravity, J. Heat Transfer – Trans. ASME 136 (2014) 021701.

[20] H. Lee, I. Mudawar, M.M. Hasan, Experimental and theoretical investigation of annular flow condensation in microgravity, Int. J. Heat Mass Transfer 61 (2013) 293–309.

[21] I. Park, L.E. O'Neill, I. Mudawar, Assessment of Body force effects in flow condensation, part I: experimental investigation of liquid film behavior for different orientations, Int. J. Heat Mass Transfer (in preparation).

[22] S.M. Kim, I. Mudawar, Universal approach to predicting heat transfer coefficient for condensing mini/micro-channel flows, Int. J. Heat Mass Transfer 56 (2013) 238–250.

[23] S.M. Kim, I. Mudawar, Review of databases and predictive methods for heat transfer in condensing and boiling mini/micro-channel flows, Int. J. Heat Mass Transfer 77 (2014) 627–652.

[24] I. Park, S.M. Kim, I. Mudawar, Experimental measurement and modeling of downflow condensation in a circular tube, Int. J. Heat Mass Transfer 57 (2013) 567–581.

[25] I. Park, H. Lee, I. Mudawar, Determination of flow regimes and heat transfer coefficient for condensation in horizontal tubes, Int. J. Heat Mass Transfer 80 (2015) 698–716.

[26] I. Park, I. Mudawar, Climbing film, flooding and falling film behavior in upflow condensation in tubes, Int. J. Heat Mass Transfer 65 (2013) 44–61.

[27] R.K. Shah, A.L. London, Laminar Flow Forced Convection in Ducts: A Source Book for Compact Heat Exchanger Analytical Data, Academic Press, New York, 1978.

[28] G.B. Wallis, One-Dimensional Two-Phase Flow, McGraw-Hill, New York, 1969.

[29] S.M. Kim, I. Mudawar, Theoretical model for annular flow condensation in rectangular micro-channels, Int. J. Heat Mass Transfer 55 (2012) 958–970.

[30] I. Mudawar, M.A. El-Masri, Momentum and heat transfer across freely-falling turbulent liquid films, Int. J. Multiphase Flow 12 (1986) 771–790.

[31] H.M. Soliman, The mist-annular transition during condensation and its influence on the heat transfer mechanism, Int. J. Multiphase Flow 12 (1986) 277–288.

[32] H.M. Soliman, On the annular-to-wavy flow pattern transition during condensation inside horizontal tubes, Can. J. Chem. Eng. 60 (1982) 475–481.

[33] J.M. Mandhane, G.A. Gregory, K. Aziz, A flow pattern map for gas–liquid flow in horizontal pipes, Int. J. Multiphase Flow 1 (1974) 537–553.

[34] Q. Chen, R.S. Amano, M. Xin, Experimental study of flow patterns and regimes of condensation in horizontal three-dimensional micro-fin tubes, Int. J. Heat Mass Transfer 43 (2006) 201–206.

[35] S.M. Kim, I. Mudawar, Flow condensation in parallel micro-channels. Part 2: heat transfer results and correlation technique, Int. J. Heat Mass Transfer 55 (2012) 984–994.

[36] G. Breber, J. Palen, J. Taborek, Prediction of horizontal tube-size condensation of pure components using flow regime criteria, J. Heat Transfer Trans. ASME 102 (1980) 471–476.

[37] H. Lamb, Hydrodynamics, sixth ed., Dover Publications, New York, 1945, p. 371.

[38] L.M. Milne-Thompson, Theoretical Hydrodynamics, forth ed., Macmillan, New York, 1960, p. 409.

[39] J.E. Galloway, I. Mudawar, CHF mechanism in flow boiling from a short heated wall – II. Theoretical CHF model, Int. J. Heat Mass Transfer 36 (1993) 2527–2540.

[40] S.M. Zivi, Estimation of steady-state steam void-fraction by means of the principle of minimum entropy production, J. Heat Transfer – Trans. ASME 86 (1964) 247–252.

[41] J.A. Shmerler, I. Mudawar, Local heat transfer coefficient in wavy free-falling turbulent liquid films undergoing uniform sensible heating, Int. J. Heat Mass Transfer 31 (1988) 67–77.

[42] J.A. Shmerler, I. Mudawar, Local evaporative heat transfer coefficient in turbulent free-falling liquid films, Int. J. Heat Mass Transfer 31 (1988) 731–742.

[43] T.H. Lyu, I. Mudawar, Statistical investigation of the relationship between interfacial waviness and sensible heat transfer to a falling liquid film, Int. J. Heat Mass Transfer 34 (1991) 1451–1464.

[44] T.H. Lyu, I. Mudawar, Determination of wave-induced fluctuations of wall temperature and convective heat transfer coefficient in the heating of a turbulent falling liquid film, Int. J. Heat Mass Transfer 34 (1991) 2521–2534.

[45] I. Mudawar, R.A. Houpt, Mass and momentum transport in smooth falling liquid films laminarized at relatively high Reynolds numbers, Int. J. Heat Mass Transfer 36 (1993) 3437–3448.

[46] I. Mudawar, R.A. Houpt, Measurement of mass and momentum transport in wavy-laminar falling liquid films, Int. J. Heat Mass Transfer 36 (1993) 4151–4162.

[47] W. Qu, I. Mudawar, S.-Y. Lee, S.T. Wereley, Experimental and computational investigation of flow development and pressure drop in a rectangular micro-channel, J. Electron. Pack. – Trans. ASME 128 (2006) 1–9.